

# A preliminary study of turbulent coherent structures and ozone air quality in Seoul using the WRF-CMAQ model at a 50 m grid spacing

Beom-Soon Han<sup>a</sup>, Jong-Jin Baik<sup>a,\*</sup>, Kyung-Hwan Kwak<sup>b</sup>

<sup>a</sup> School of Earth and Environmental Sciences, Seoul National University, Seoul, South Korea

<sup>b</sup> School of Natural Resources and Environmental Science, Kangwon National University, Chuncheon, South Korea

## ARTICLE INFO

### Keywords:

Ozone air quality  
Turbulent coherent structure  
Convective structures  
WRF-CMAQ model  
Large-eddy simulation

## ABSTRACT

The effects of turbulent coherent structures on daytime ozone air quality in Seoul, South Korea are investigated through a case study using the Weather Research and Forecasting-Community Multiscale Air Quality (WRF-CMAQ) model at a horizontal grid spacing of 50 m. In Seoul, sea breeze and convective structures develop in the daytime. Due to the different wind directions above and below the planetary boundary layer (PBL) top, eddies are formed at the PBL top when updrafts related to convective structures reach above the PBL top. Air at lower level, which has higher concentrations of O<sub>3</sub> precursors and lower O<sub>3</sub> concentration than air at upper level, is transported upward by convective structures and eddies at the PBL top. Some of the transported air reaches above the PBL top, resulting in the vigorous chemical production of O<sub>3</sub> above the PBL top in the afternoon. An integrated process rate analysis is performed to examine the impacts of turbulent coherent structures on O<sub>3</sub> concentration in detail. The chemical production of O<sub>3</sub> generally appears in updraft areas except near the surface because O<sub>3</sub> precursors at lower level are transported by updrafts. Below the height of ~1 km, the horizontal advection of air from other areas to updraft areas increases O<sub>3</sub> concentration in updraft areas because O<sub>3</sub> concentration in updraft areas is generally lower than that in other areas. Slightly above the PBL top, air with low O<sub>3</sub> concentration diverges from updraft areas and air with high O<sub>3</sub> concentration at upper level is transported downward by downdrafts around updraft areas.

## 1. Introduction

Urban air pollution is one of the important environmental problems in modern society. In urban areas, primary pollutants such as NO<sub>x</sub> (= NO + NO<sub>2</sub>) and volatile organic compounds (VOCs) are emitted directly from motor vehicles, factories, and other anthropogenic sources. Additionally, secondary pollutants such as ozone (O<sub>3</sub>) are formed in urban atmosphere. Since exposure to O<sub>3</sub> poses serious health hazards in humans including respiratory damages, many countries define exposure limits for O<sub>3</sub>. For example, an exposure limit for 8-hr averaged O<sub>3</sub> concentration in South Korea is 60 ppb. Many observations (Zaveri et al., 2003; Zhang et al., 2008; Mao et al., 2010; Stauffer et al., 2015; Sullivan et al., 2019) and numerical simulations (Civerolo et al., 2007; Hogrefe et al., 2007; Tao et al., 2018) have also been performed to investigate dispersion and chemical reactions of O<sub>3</sub> in urban areas.

Previous studies have shown that O<sub>3</sub> air quality in urban areas is affected by regional scale flows, such as urban breezes and land/sea breezes. Ryu et al., 2013a investigated the impacts of urban breezes on

O<sub>3</sub> concentration in the Seoul area. They found that the urban heat island increases the boundary layer height in the urban area and induces a convergent flow toward the urban area (urban breeze). As a result, NO<sub>x</sub> in the urban boundary layer is diluted and air with low NO<sub>x</sub> and high VOCs concentrations is transported from the surrounding areas with dense vegetation to the urban area, resulting in an increased O<sub>3</sub> concentration in the urban area. As anthropogenic heat in the urban area becomes stronger, the urban breeze is enhanced and O<sub>3</sub> concentration increases in the urban area (Ryu et al., 2013b). Zhang et al. (2007) showed that high O<sub>3</sub> concentration in the Houston area (a coastal urban area) can be caused by sea/land breezes and associated recirculation of reactive pollutants. The land breeze transports reactive pollutants including O<sub>3</sub> precursors from the urban area to the sea, and O<sub>3</sub> is formed over the sea. Then, air with high O<sub>3</sub> concentration over the sea is transported to the urban area by the sea breeze, resulting in high O<sub>3</sub> concentration in the urban area. Loughner et al. (2011, 2014) investigated the effects of bay breeze on vertical dispersion of O<sub>3</sub> in the Washington and Baltimore area. They found that O<sub>3</sub> near the surface is

\* Corresponding author. School of Earth and Environmental Sciences, Seoul National University, Seoul 08826, South Korea.

E-mail address: jjbaik@snu.ac.kr (J.-J. Baik).

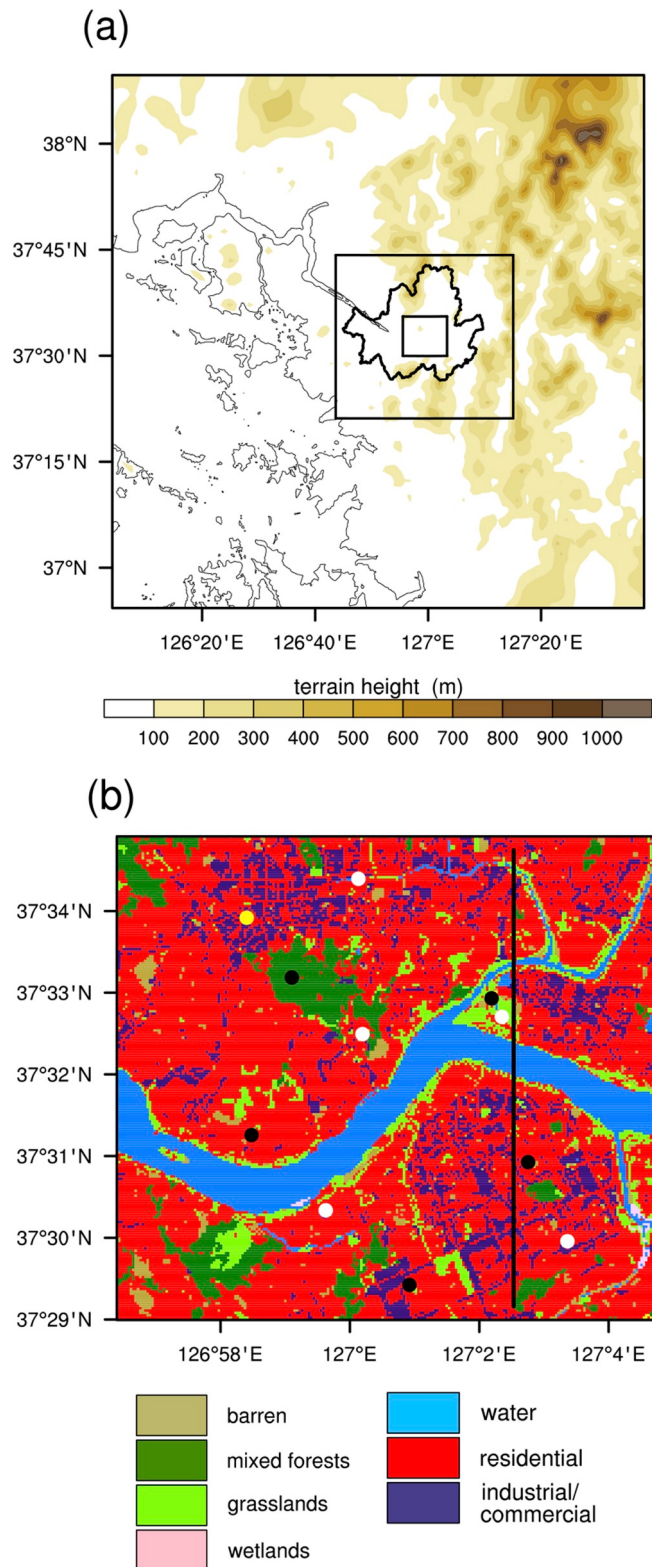


**Fig. 1.** (a) Domains of CMAQ simulation with terrain height and (b) land-use/land-cover in the 50 m domain. The boundary of Seoul is indicated by the black solid line in (a). The white and black dots in (b) indicate the locations of air quality monitoring stations (AQMSs) and automatic weather stations (AWSs), respectively. The yellow dot in (b) indicates the location of Jung-gu AQMS. The black solid line in (b) indicates the vertical cross-section line for Figs. 6, 7b and 11. (For interpretation of the references to colour in this figure legend, the reader is referred to the Web version of this article.)

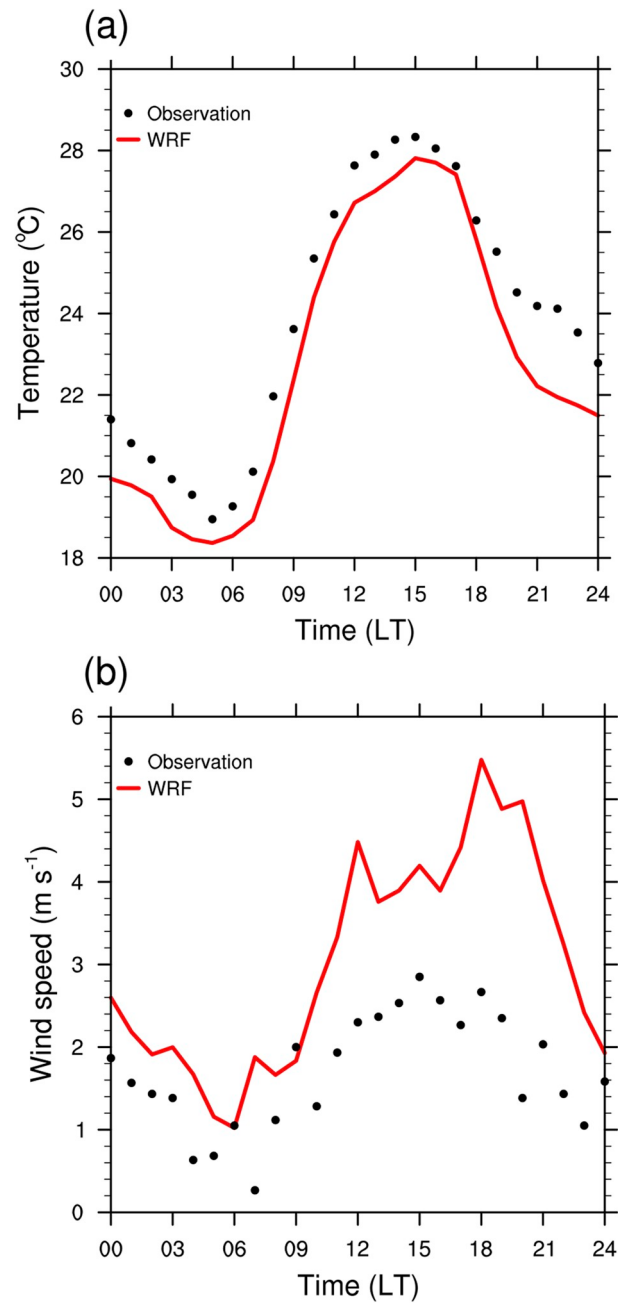


**Fig. 2.** Diurnal variations of the simulated (lines) and observed (dots) (a) air temperatures and (b) wind speeds near the surface averaged over the 5 AWSs (black dots in Fig. 1b) on 5 June 2010.

transported upward above the urban boundary layer by the bay breeze circulation. The transported O<sub>3</sub> is advected horizontally to the surrounding areas and affects air quality there.

While the aforementioned simulation studies show that regional scale flows affect reactive pollutant dispersion in urban areas, smaller-scale turbulent flows can also significantly affect reactive pollutant dispersion. Particularly, convective structures, which is one of the smaller-scale turbulent coherent structures, can greatly affect dispersion and chemical reactions of reactive pollutants in the convective boundary layer (CBL). Schumann (1989) examined the effects of convective structures on reactive pollutant dispersion in the CBL over a flat surface. Updrafts and downdrafts related to convective structures transport the upward-diffused (emitted at the surface) and downward-diffused (initially included in air) reactive pollutants, respectively. As a result,

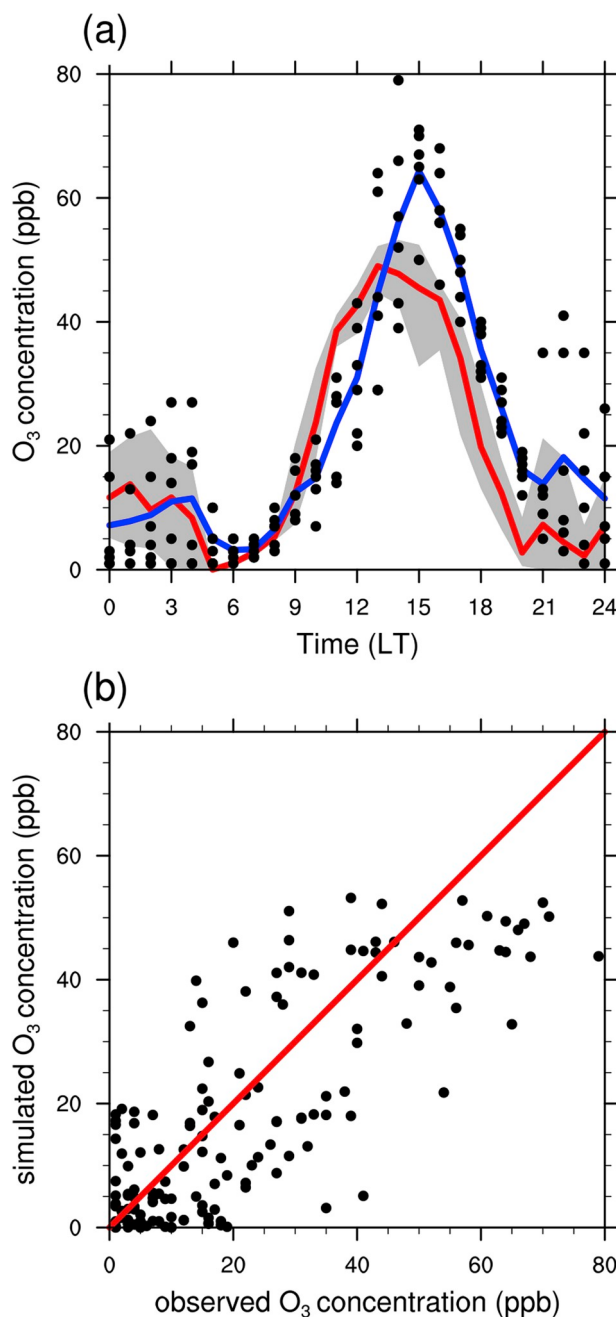


**Fig. 3.** (a) Diurnal variations of the simulated and observed  $O_3$  concentrations near the surface on 5 June 2010. The dots indicate the observed  $O_3$  concentrations at the 6 AQMSs (5 white dots and one yellow dot in Fig. 1b), and the shading indicates the range of the simulated  $O_3$  concentration at the locations corresponding to the observation sites. The blue and red lines indicate the observed and simulated  $O_3$  concentrations, respectively. (b) Scatter plot of the simulated  $O_3$  concentrations versus the observed  $O_3$  concentrations on 5 June 2010. (For interpretation of the references to colour in this figure legend, the reader is referred to the Web version of this article.)

concentrations of the upward-diffused and downward-diffused reactive pollutants are high in updraft and downdraft areas, respectively; that is, convective structures in the CBL spatially segregate the upward-diffused and downward-diffused reactive pollutants and reduce the chemical reaction rate of the reactive pollutants (Vilà-Guerau de Arellano et al., 2004). Han et al. (2019) investigated the effects of an idealized building array on convective structures and reactive pollutant dispersion in the CBL. When background wind exists, the building array decreases wind

speed in the CBL. Since wind speed in the free atmosphere barely changes, wind shear at and near the CBL top is enhanced. The enhanced wind shear increases turbulent intensity and induces vigorous reactive pollutant exchange at and near the CBL top. Increasing the building height of the building array enhances wind shear and turbulent flows at and near the CBL top, resulting in more vigorous reactive pollutant exchange at and near the CBL top.

Previous studies generally investigated the effects of convective structures on dispersion and chemical reactions of reactive pollutants under ideal conditions. Realistic conditions, such as real morphology, spatially inhomogeneous pollutant emission, and synoptic weather forcing, can significantly change convective structures and dispersion and chemical reactions of reactive pollutants. However, to the authors' knowledge, there is no study investigating the effects of convective structures on air quality in real urban areas. In this study, the effects of turbulent coherent structures, such as convective structures, on dispersion and chemical reactions of  $O_3$  in a real urban area are investigated. In section 2, the model and simulation design are described and the model simulation is validated. The results are presented and discussed in section 3. In section 4, a summary and conclusions are given.

## 2. Methodology and validation

### 2.1. Meteorology model

The Weather Research and Forecasting (WRF) model version 3.8.1 (Skamarock et al., 2008) is used as a meteorology model in this study. Two-way nested five domains with horizontal grid spacings of 31.25 km, 6.25 km, 1.25 km, 0.25 km, and 50 m are considered. There are 72 vertical layers, and the number of vertical layers below 2 km is 41. The lowest vertical grid spacing is  $\sim 43$  m, and the vertical grid spacing increases with height. The Dudhia shortwave radiation scheme (Dudhia, 1989), the Rapid Radiative Transfer Model (RRTM) longwave radiation scheme (Mlawer et al., 1997), the Noah land surface model (Chen and Dudhia, 2001), and the WRF single-moment 6-class microphysics scheme (Hong and Lim, 2006) are used. The Kain-Fritsch scheme (Kain, 2004) is used to parameterize subgrid-scale cumulus convection, and it is used only for the outermost two domains with horizontal grid spacings of 31.25 and 6.25 km. The Seoul National University Urban Canopy Model (SNUUCM) (Ryu et al., 2011) is used to represent urban effects on meteorological variables. In the outermost three domains with horizontal grid spacings of 31.25, 6.25, and 1.25 km, the Yonsei University (YSU) planetary boundary layer (PBL) scheme (Hong et al., 2006) is used.

In the innermost two domains with horizontal grid spacings of 0.25 km and 50 m, the WRF model is run in the large-eddy simulation (LES) mode to accurately simulate turbulent flows. According to Rai et al. (2017) and Cuchiara and Rappenglück (2018), turbulent quantities in the PBL calculated using results of the WRF-LES model are well matched with observed turbulent quantities, indicating that the WRF-LES model accurately reproduces turbulent flows in the PBL. The 1.5-order turbulent kinetic energy closure is used in the LES mode of the WRF model (Deardorff, 1980; Moeng, 1984) to calculate eddy diffusivities for heat and momentum. Unless otherwise noted, data for the innermost domain with a horizontal grid spacing of 50 m are analyzed in this study.

Following Ryu and Baik (2013), the Shuttle Radar Topography Mission (SRTM) data with a 3 s resolution ( $\sim 90$  m) (Farr et al., 2007) are used for topography data and geographic information system data with a 4 m resolution produced by the Korea Ministry of Environment are used for high-resolution land-use/land-cover data (Fig. 1b). The gridded anthropogenic heat data over South Korea estimated from regression relations between anthropogenic air pollutant emissions and anthropogenic heat flux (Lee and Kim, 2015) are used in this study. The WRF model is integrated for 39 h from 0900 LT (= UTC + 9 h) 4 June to 2400 LT 5 June 2010. For the initial and boundary conditions, the National

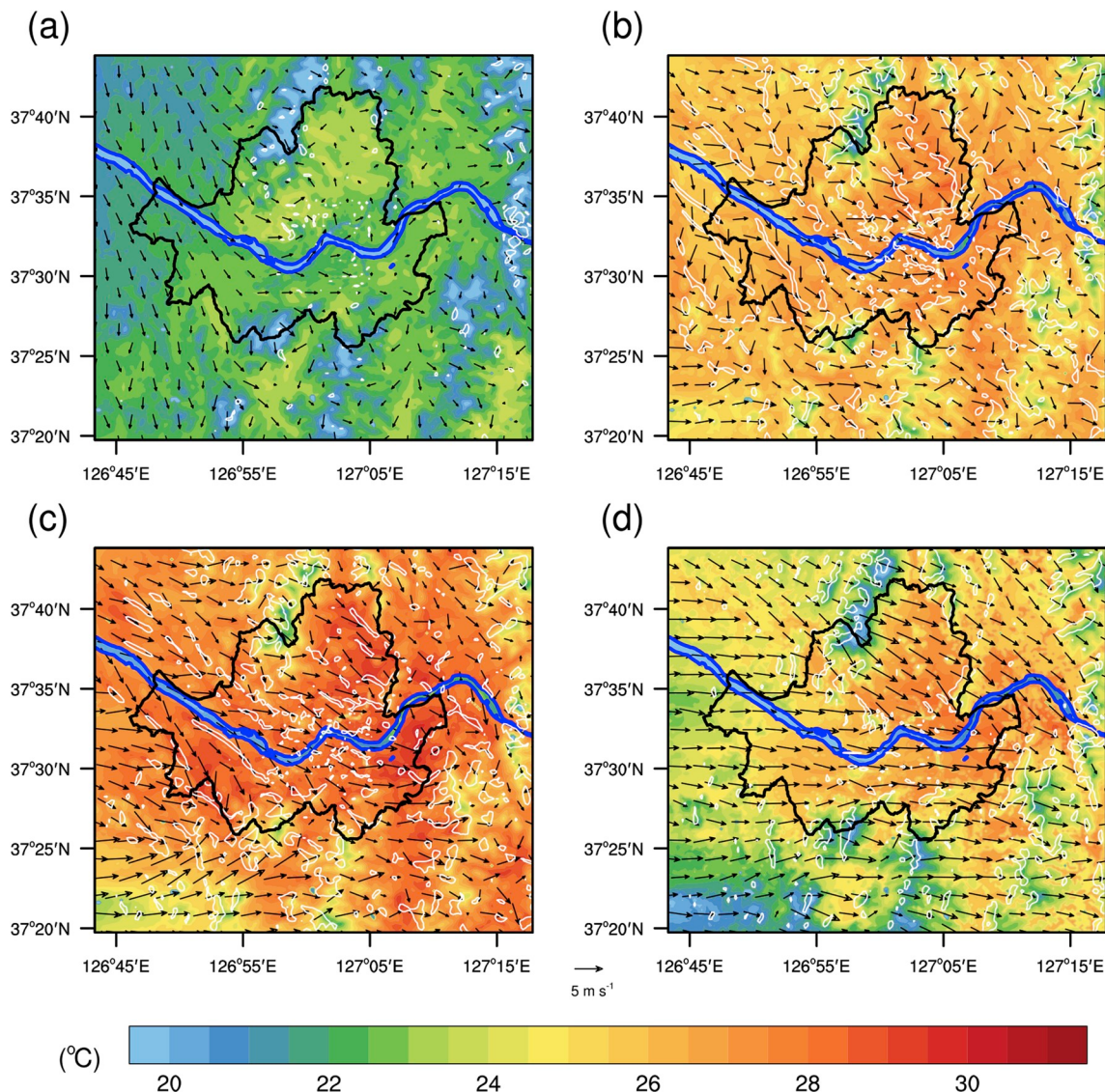


**Fig. 4.** Fields of air temperature at 2 m and horizontal wind vector at 10 m in the 0.25 km domain at (a) 0900, (b) 1200, (c) 1500, and (d) 1800 LT. The white contour lines represent the contours of vertical velocity with  $0.5 \text{ m s}^{-1}$  at the second lowest model level ( $z \sim 100 \text{ m}$ ), and the blue lines indicate the Han River. (For interpretation of the references to colour in this figure legend, the reader is referred to the Web version of this article.)

Centers for Environmental Prediction (NCEP) final analysis data ( $1^\circ \times 1^\circ$ ) are used.

## 2.2. Air quality model

The Community Multiscale Air Quality (CMAQ) model version 5.2 (Byun and Schere, 2006) is coupled with the WRF-LES model to simulate air quality. One-way nested three domains with horizontal grid spacings of 1.25 km, 0.25 km, and 50 m are considered for air quality simulation (hereafter called the 1.25 km, 0.25 km, and 50 m domains, respectively), and the 50 m domain covers the central area of Seoul, the largest city in South Korea (Fig. 1a). Unless otherwise noted, data of the 50 m domain are analyzed in the present study. Note that the 1.25 km, 0.25 km, and 50 m domains for air quality simulation correspond to domains with horizontal grid spacings of 1.25 km, 0.25 km, and 50 m for meteorology simulation, respectively. The study area is highly urbanized, with the Yellow Sea to its west. Therefore, sea breeze blowing from the Yellow Sea can affect air quality of the study area. There are 5 automatic weather stations (AWSs, black dots in Fig. 1b) and Fig. 6 air quality monitoring stations (AQMSs, 5 white dots and one yellow dot in Fig. 1b)

in the 50 m domain. The vertical layers in the air quality simulation are the same as those in the meteorology simulation.

The Statewide Air Pollution Research Center (SAPRC) version 2007 chemical mechanism for gas-phase chemistry (Carter, 2010) and the sixth-generation modal CMAQ aerosol module (AERO6) for the aerosol process (Appel et al., 2013) are used. The eddy diffusivity for heat calculated from the WRF-LES model is used as the eddy diffusivity for reactive pollutants in the CMAQ model simulation. The PBL height calculated following Hong et al. (2006) using the WRF-LES model simulation data is used as the PBL height in the CMAQ model simulation. The CMAQ model is integrated for 39 h starting from 0900 LT 4 June 2010, and the last 24-h data (data of 5 June 2010) are analyzed. During the simulation period, synoptic weather forcing is weak, so the amount of long-range transported pollutants coming into Seoul is small. Therefore, we speculate that a rather short spin-up time (15 h) would be enough to simulate pollutant concentrations in this study. For the initial and boundary conditions of the 1.25 km domain, the default concentration profiles of the CMAQ modeling system are used. To estimate anthropogenic and biogenic pollutant emissions, the Sparse Matrix Operator Kernel Emissions (SMOKE) system (Houyoux et al., 2000) and

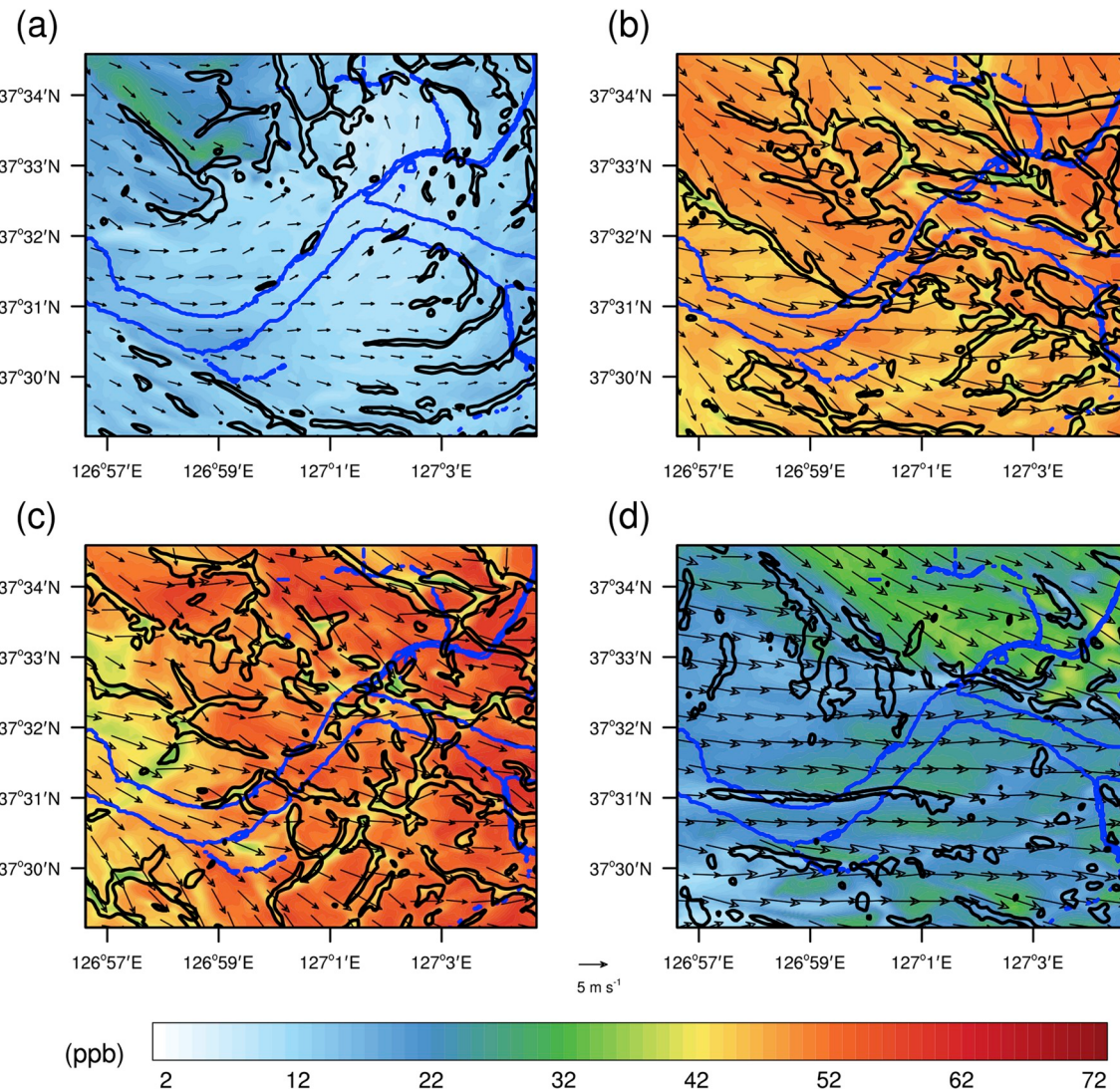


**Fig. 5.** Fields of  $O_3$  concentration and horizontal wind vector at the second lowest model level ( $z \sim 100$  m) at (a) 0900, (b) 1200, (c) 1500, and (d) 1800 LT. The black contour lines represent the contours of vertical velocity with  $0.5\text{ m s}^{-1}$ . The blue lines indicate the Han River and its tributaries. (For interpretation of the references to colour in this figure legend, the reader is referred to the Web version of this article.)

the Model of Emissions of Gases and Aerosols from Nature (MEGAN) (Guenther et al., 2006) are used, respectively. For an anthropogenic emission inventory with a horizontal resolution of 1 km in the present study, the 2007 Clean Air Policy Support System (CAPSS) data (Moon et al., 2006) updated by Ryu et al., 2013a are used. Various data (e.g., emission measurement data, amount of fuel combustion data, and vehicle number data) from approximately 150 organizations in South Korea were utilized to generate the CAPSS data. For example, activity data for mobile emission sources were compiled by the Korea Automobile Manufacturers Association (KAMA), the Korea Association for National Gas Vehicles (KANGV), and other organizations (Lee et al., 2011). The anthropogenic emissions are spatially and temporally allocated following Kim et al. (2008) in the 1.25 km domain. In the 0.25 km and 50 m domains, the bilinear interpolation method is used to estimate anthropogenic emissions from the emission inventory with a horizontal resolution of 1 km.

### 2.3. Model validation

The simulated near-surface air temperature and wind speed are validated using the observation data from the 5 AWSs operated by the Korea Meteorological Administration. The simulated air temperatures

and wind speeds corresponding to the locations of the 5 AWSs are calculated using the bilinear interpolation method and are compared with the observation data. Fig. 2a shows the diurnal variations of the simulated and observed near-surface air temperatures averaged over the 5 AWSs on 5 June 2010. The WRF-LES model slightly underestimates the air temperature near the surface, especially at night, but the diurnal variation pattern of the simulated air temperature is similar to that of the observed air temperature. The mean bias and root-mean-square error of the simulated air temperature are  $-1.1$  and  $1.5^\circ\text{C}$ , respectively. Fig. 2b shows the diurnal variations of the simulated and observed near-surface wind speeds averaged over the 5 AWSs on 5 June 2010. The WRF-LES model overestimates the wind speed near the surface but captures the diurnal variation pattern of the observed wind speed. In urban areas, the wind speed decreases in the presence of buildings. However, this effect is not well represented in an urban canopy model. This seems to be related to the overestimation of the simulated near-surface wind speed. The mean bias and root-mean-square error of the simulated wind speed are  $1.3$  and  $2.0\text{ m s}^{-1}$ , respectively.

The simulated near-surface  $O_3$  concentration is validated using the observation data from the 6 AQMSs operated by the Korea Environmental Corporation. The simulated  $O_3$  concentrations corresponding to the locations of the 6 AQMSs are calculated using the bilinear

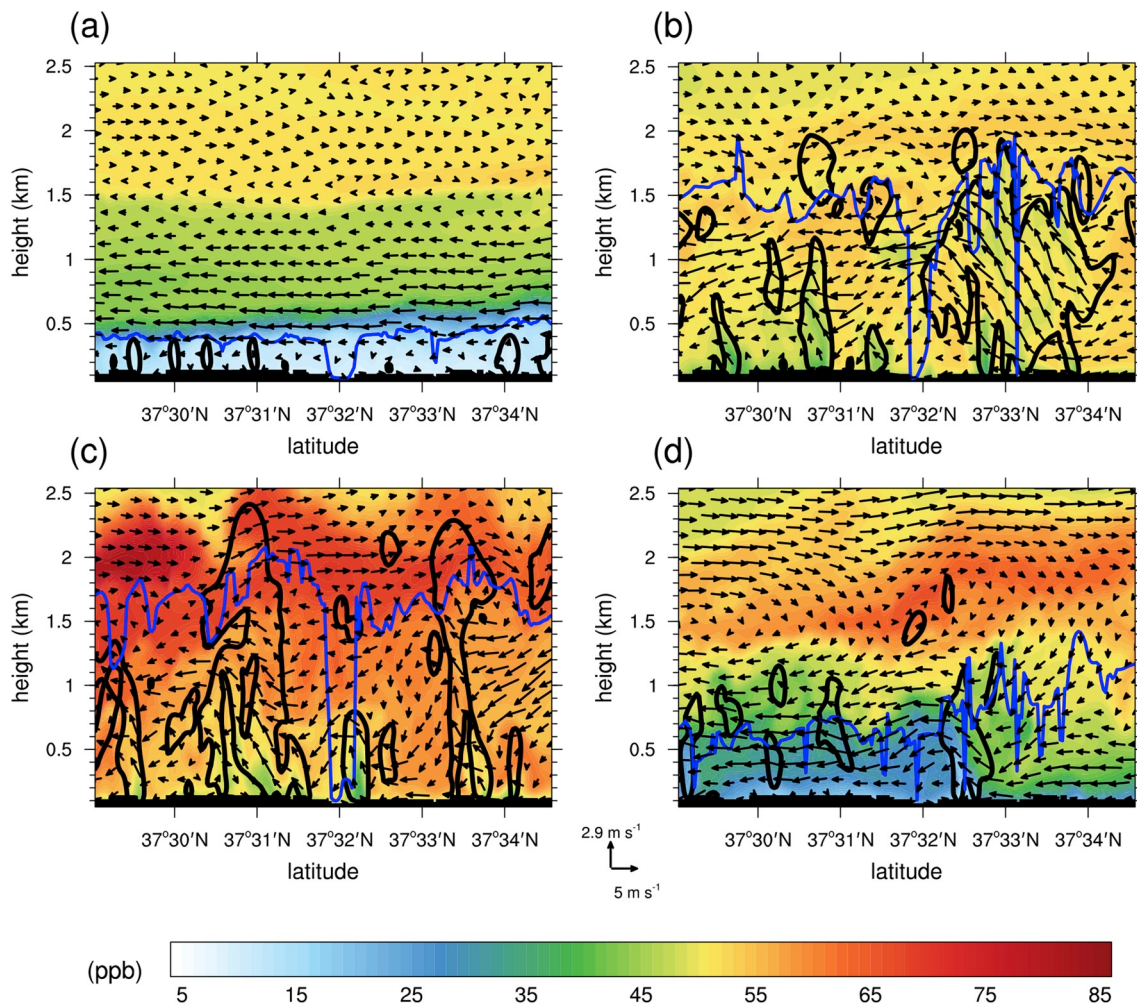


**Fig. 6.** Vertical cross-sections of  $O_3$  concentration and wind vector at (a) 0900, (b) 1200, (c) 1500, and (d) 1800 LT along the black solid line in Fig. 1b. The black contour lines represent the contours of vertical velocity with  $0.5 \text{ m s}^{-1}$ , and the blue lines represent the PBL height. (For interpretation of the references to colour in this figure legend, the reader is referred to the Web version of this article.)

interpolation method and are compared with the observation data. Fig. 3a shows the diurnal variations of the simulated and observed  $O_3$  concentrations near the surface on 5 June 2010. In Fig. 3a, the dots represent the observed  $O_3$  concentrations at the 6 AQMSs, and the shading represents the range of simulated  $O_3$  concentrations at the locations corresponding to the observation sites. The blue and red lines represent the observed and simulated  $O_3$  concentrations averaged over the locations of the 6 AQMSs, respectively. Although the daily maximum averaged  $O_3$  concentrations in the simulation and observation appear at slightly different times (1300 LT in the simulation and 1500 LT in the observation), the diurnal variation patterns of the simulated and observed  $O_3$  concentrations are generally similar. Since the resolution of the emission inventory (1 km) is larger than the horizontal grid spacing of the 50 m domain, pollutant emission in the 50 m domain is not adequately resolved. This seems to be related to the difference between the simulated and observed  $O_3$  concentrations. Future studies considering emission inventories with higher resolutions are needed. The mean bias and root-mean-square error of the simulated  $O_3$  concentration are  $-3.8$  and  $13 \text{ ppb}$ , respectively. Fig. 3b shows a scatter plot of the simulated  $O_3$  concentration versus the observed  $O_3$  concentration on 5 June 2010. The simulated  $O_3$  concentration is well correlated with the observed  $O_3$  concentration. The correlation between the simulated and observed  $O_3$  concentrations is  $0.80$ . Additionally, the simulated near-surface  $NO_2$  concentration is also validated using the observation data from the 6 AQMSs. The mean bias and root-mean-square error of the

simulated  $NO_2$  concentration are  $-10$  and  $16 \text{ ppb}$ , respectively. The correlation between the simulated and observed  $NO_2$  concentrations is  $0.35$ . The simulated  $NO_2$  concentration is generally lower than the observed  $NO_2$  concentration, but the increase of the observed  $NO_2$  concentration at rush hours also appears in the simulation results. This underestimation of the simulated  $NO_2$  concentration seems to be caused by the low resolution of the emission inventory.

### 3. Results and discussion

#### 3.1. Turbulent flows and $O_3$ air quality

In this subsection, the development of convective structures in Seoul is investigated and their effects on  $O_3$  air quality are analyzed. During the simulation period, the synoptic weather forcing is weak and weather is calm and sunny. Accordingly, there is a well-developed sea breeze blowing from the Yellow Sea to Seoul, which transports air from the west to northwest of Seoul. Also, strong surface heating during the simulation period increases the temperature of air near the surface. The heated air rises upward and forms a convective structure, which has a great influence on flow and pollutant dispersion. Fields of air temperature at 2 m and horizontal wind vector at 10 m in the 0.25 km domain are shown in Fig. 4 to present the sea breeze and convective structures. The white contour lines represent the contours of vertical velocity with  $0.5 \text{ m s}^{-1}$  at the second lowest model level (near the surface,  $z \sim 100 \text{ m}$ ,  $z$ : height

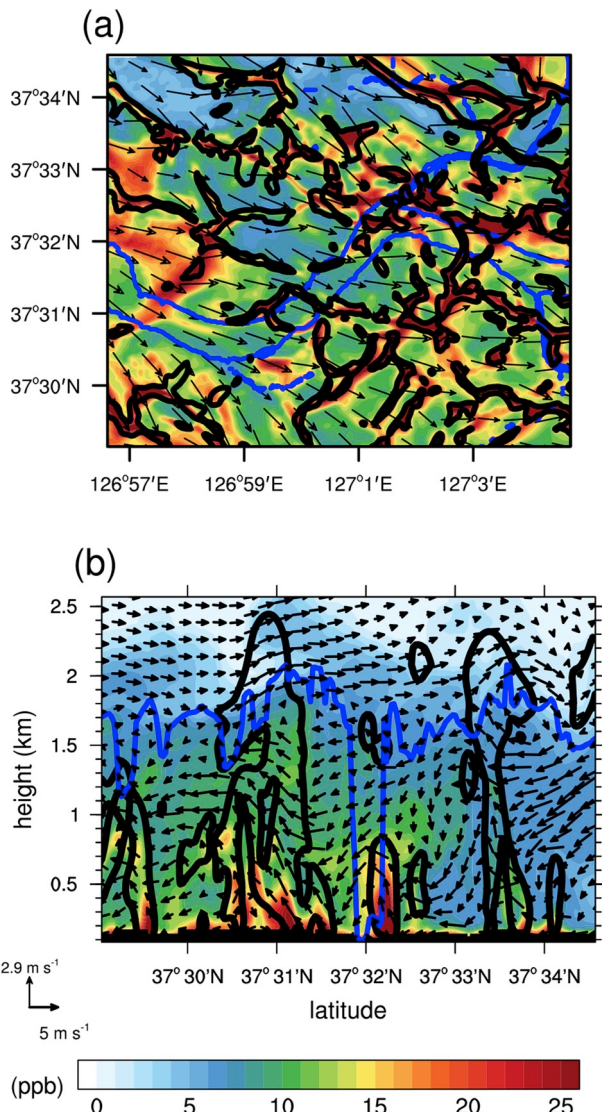


**Fig. 7.** (a) Fields of NO<sub>x</sub> concentration and horizontal wind vector at the second lowest model level ( $z \sim 100$  m) at 1500 LT. (b) Vertical cross-sections of NO<sub>x</sub> concentration and wind vector along the black solid line in Fig. 1b at 1500 LT. The black contour lines in (a) and (b) represent the contours of vertical velocity with  $0.5 \text{ m s}^{-1}$ . The blue lines in (a) indicate the Han River and its tributaries, and the blue lines in (b) represent the PBL height. (For interpretation of the references to colour in this figure legend, the reader is referred to the Web version of this article.)

above the sea level), and the blue lines indicate the Han River. At 0900 LT, the horizontal wind in Seoul is weak and convective structures due to surface heating appear in the central area of Seoul. Updrafts related to convective structures in the central area of Seoul are weak because of weak surface heating (Fig. 4a). At 1200 and 1500 LT, the sea breeze blows in Seoul and the horizontal wind speed increases (Fig. 4b and c). The sea breeze also affects the wind direction in Seoul, which becomes closer to being westerly as a result. Convective structures are developed in Seoul and the surrounding areas, and updrafts related to convective structures are enhanced. Due to enhanced updrafts related to convective structures, air converges to updraft areas. At 1800 LT, the sea breeze still blows in Seoul and becomes further enhanced, but convection in Seoul and updrafts related to convective structures are weakened (Fig. 4d). Updraft areas at 1800 LT are significantly reduced compared to those at 1500 LT.

These sea breeze and convective structures affect O<sub>3</sub> concentration in

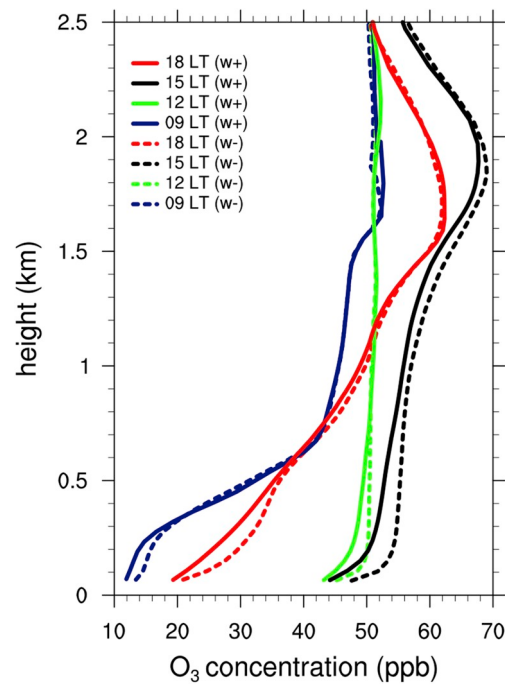


**Fig. 8.** Vertical profiles of area-averaged O<sub>3</sub> concentration at 0900, 1200, 1500, and 1800 LT. The solid and dashed lines represent the O<sub>3</sub> concentrations averaged over updraft areas larger than  $0.1 \text{ m s}^{-1}$  ( $w+$ ) and downdraft areas smaller than  $-0.1 \text{ m s}^{-1}$  ( $w-$ ), respectively. (For interpretation of the references to colour in this figure legend, the reader is referred to the Web version of this article.)

Seoul significantly. Fields of O<sub>3</sub> concentration and horizontal wind vector at the second lowest model level at 0900, 1200, 1500, and 1800 LT are shown in Fig. 5. The black contour lines represent the contours of vertical velocity with  $0.5 \text{ m s}^{-1}$ . Updrafts related to convective structures appear, especially in the daytime. O<sub>3</sub> concentration in updraft areas is lower than that in other areas because air at lower level, which has higher NO<sub>x</sub> concentration than air at upper level, is transported upward and induces O<sub>3</sub> decomposition. This air with low O<sub>3</sub> concentration in updraft areas is transported upward and lowers O<sub>3</sub> concentration in updraft areas at upper level. The lower O<sub>3</sub> concentration in updraft areas is clearly seen at 1200 and 1500 LT (Fig. 5b and c) because convective structures are well-developed in the daytime. In the morning and late afternoon, the lower O<sub>3</sub> concentration in updraft areas is not clearly seen because convection in Seoul is weak (Fig. 5a and d).

The vertical cross-sections of O<sub>3</sub> concentration and wind vector at 0900, 1200, 1500, and 1800 LT along the black solid line in Fig. 1b are shown in Fig. 6. The black contour lines represent the contours of vertical velocity with  $0.5 \text{ m s}^{-1}$ . The blue lines represent the PBL height. The PBL height at and near  $37^{\circ} 32.0^{\prime}$ N are low because the Han River exists there, which lowers the surface temperature. At 0900 LT, O<sub>3</sub> concentration below the PBL top does not change much with height and vertical motions related to convective structures are weak (Fig. 6a). Therefore, the effects of convective structures on O<sub>3</sub> concentration are small. At 1200 LT, vertical motions due to convective structures are strengthened and updrafts related to convective structures transport air at lower level upward, which has lower O<sub>3</sub> concentration than air at upper level (Fig. 6b). Additionally, a clockwise-rotating eddies at the PBL top appear at  $37^{\circ} 34.1^{\prime}$ N and mix air above and below the PBL top. At 1200 and 1500 LT, wind directions above and below the PBL top are different (southeasterly wind above the PBL top and northwesterly wind below it). Therefore, wind shear at the PBL top is great and clockwise-rotating eddies can be formed when updrafts related to convective structures reach above the PBL top. It seems that different wind directions at upper and lower levels of the sea breeze circulation are

**Table 1**

Mean bias (MB) and root-mean-square error (RMSE) of the simulated O<sub>3</sub> and NO<sub>2</sub> concentrations and correlation (CORR) between the observed and simulated O<sub>3</sub> and NO<sub>2</sub> concentrations in the 1.25 km, 0.25 km, and 50 m domains. The units of the MB and RMSE are ppb, and the correlation is unitless.

	1.25 km domain			0.25 km domain			50 m domain		
	MB	RMSE	CORR	MB	RMSE	CORR	MB	RMSE	CORR
O <sub>3</sub>	-1.2	13	0.76	-2.9	12	0.81	-3.8	13	0.80
NO <sub>2</sub>	-14	19	0.31	-11	16	0.38	-10	16	0.35

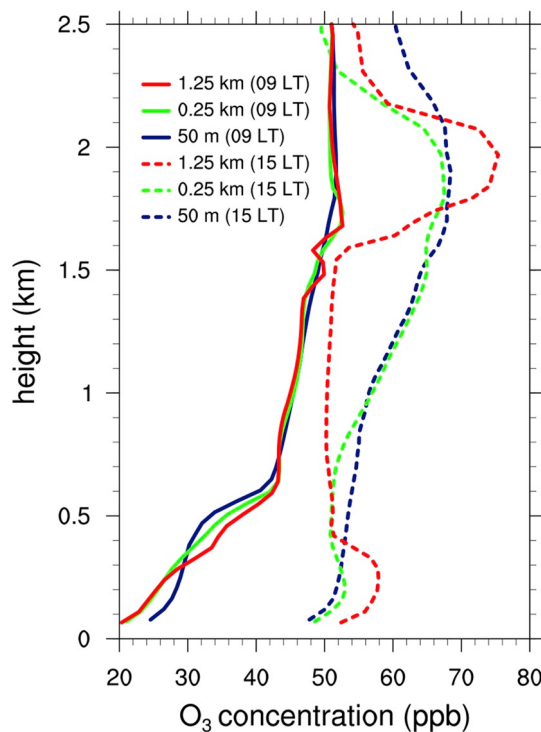


**Fig. 9.** Vertical O<sub>3</sub> concentration profiles at the location of Jung-gu AQMS indicated by the yellow dot in Fig. 1b at 0900 and 1500 LT from the results of the 1.25 km, 0.25 km, and 50 m domains. (For interpretation of the references to colour in this figure legend, the reader is referred to the Web version of this article.)

largely responsible for the different wind directions above and below the PBL top. The strengthened mixing of air caused by the strong wind shear at the PBL top has also been reported in a study of ideal convective boundary layer (Han et al., 2019). At 1500 LT, convective structures and associated vertical motions are further developed and eddies at the PBL top appear more frequently (e.g., an eddy at 37° 33.8'N) (Fig. 6c). At 1800 LT, vertical motions related to convective structures are weakened and eddies at the PBL top do not appear (Fig. 6d). This seems to be because the wind directions just above and below the PBL top are similar (northwesterly wind just above and below the PBL top). In the region between  $z \sim 1.3$  km and  $z \sim 2.3$  km, O<sub>3</sub> concentration is high because O<sub>3</sub> formed in the afternoon still remains. Long-range transport of O<sub>3</sub> contributes little to this high O<sub>3</sub> concentration between  $z \sim 1.3$  km and  $z \sim 2.3$  km from 1200 LT to 1800 LT due to the generally low wind speed at and near the PBL top.

The effects of turbulent coherent structures on NO<sub>x</sub> concentration are also analyzed. Fig. 7 shows fields of NO<sub>x</sub> concentration and horizontal wind vector at the second lowest model level and the vertical cross-sections of NO<sub>x</sub> concentration and wind vector along the black solid line in Fig. 1b at 1500 LT. The black contour lines represent the contours of vertical velocity with 0.5 m s<sup>-1</sup>. Contrary to O<sub>3</sub> concentration, NO<sub>x</sub> concentration in updraft areas is higher than that in other areas because updrafts transport air at lower level upward, which has higher NO<sub>x</sub>

concentration than air at upper level (Fig. 7a). The high NO<sub>x</sub> concentration in updraft areas corresponds to low O<sub>3</sub> concentration in updraft areas because the air transported from lower level has lower O<sub>3</sub> concentration than air at upper level. The northern part of the central area of Seoul exhibits lower NO<sub>x</sub> concentration than that in the southern part of the central area of Seoul. This is because the westerly to northwesterly sea breeze transports air with low NO<sub>x</sub> concentration from the northwest of Seoul to the central area of Seoul. The eddy at 37° 34.1'N also mixes air above and below the PBL top, and NO<sub>x</sub> and other O<sub>3</sub> precursors below the PBL top are transported upward above the PBL top (Fig. 7b).

To quantitatively compare O<sub>3</sub> concentration in updraft and downdraft areas, the vertical profiles of area-averaged O<sub>3</sub> concentration at 0900, 1200, 1500, and 1800 LT are shown in Fig. 8. The solid and dashed lines represent the O<sub>3</sub> concentrations averaged over updraft areas larger than 0.1 m s<sup>-1</sup> ( $w_+$ ) and downdraft areas smaller than -0.1 m s<sup>-1</sup> ( $w_-$ ), respectively. Below  $z \sim 0.3$  km, the area-averaged O<sub>3</sub> concentration in downdraft areas is higher than that in updraft areas because downdrafts transport air at upper level downward, which has higher O<sub>3</sub> concentration than air at lower level and updrafts transport air at lower level upward, which has lower O<sub>3</sub> concentration than air at upper level. The difference between the area-averaged O<sub>3</sub> concentrations in updraft and downdraft areas decreases with height, indicating that the effects of vertical motions related to convective structures on O<sub>3</sub> concentration decrease with height. The differences between the area-averaged O<sub>3</sub> concentrations averaged in the 5 lowest model levels ( $z < \sim 0.24$  km) are 1.9, 2.8, 4.1, and 3.6 ppb at 0900, 1200, 1500, and 1800 LT, respectively. The difference between the area-averaged O<sub>3</sub> concentrations averaged in the 5 lowest model levels increases from 0900 LT to 1500 LT due to the development of convective structures. It does not change much from 1500 LT to 1800 LT, indicating that the effects of convective structures on O<sub>3</sub> concentration at lower level are still sustained in the late afternoon.

From 0900 LT to 1200 LT, the area-averaged O<sub>3</sub> concentrations in updraft and downdraft areas below  $z \sim 0.5$  km are increased significantly by the chemical production of O<sub>3</sub> because O<sub>3</sub> precursors are abundant at lower level due to the low PBL height. From 1200 LT to 1500 LT, the area-averaged O<sub>3</sub> concentrations at and near the PBL top ( $z \sim 1.2$ –2.3 km) increase significantly, and the maximum area-averaged O<sub>3</sub> concentration at 1500 LT appears at  $z \sim 1.9$  km, slightly above the PBL top. This is because O<sub>3</sub> precursors are transported upward by updrafts related to convective structures and clockwise-rotating eddies at the PBL top. As a result, the chemical production of O<sub>3</sub> becomes vigorous at and above the PBL top. Furthermore, the wind speed at and near the PBL top is generally lower than the wind speed above and below the PBL top, thus O<sub>3</sub> can accumulate at and near the PBL top. From 1500 LT to 1800 LT, the decrease of the area-averaged O<sub>3</sub> concentrations above  $z \sim 1.3$  km is small, indicating that O<sub>3</sub> formed in the afternoon at upper level can stay in the atmosphere for a long time. If this O<sub>3</sub> at upper level stays until the next day, it subsides into the PBL when the PBL grows, worsening air quality.

To examine the effects of horizontal model resolution on model performance, the mean bias, root-mean-square error, and correlation are calculated using the simulated O<sub>3</sub> and NO<sub>2</sub> concentrations in the 1.25 km, 0.25 km, and 50 m domains (Table 1). Note that the YSU PBL scheme is used in the domain with a horizontal grid spacing of 1.25 km and the LES mode is used in the domains with horizontal grid spacings of 0.25 km and 50 m. For O<sub>3</sub> concentration, the mean bias, root-mean-

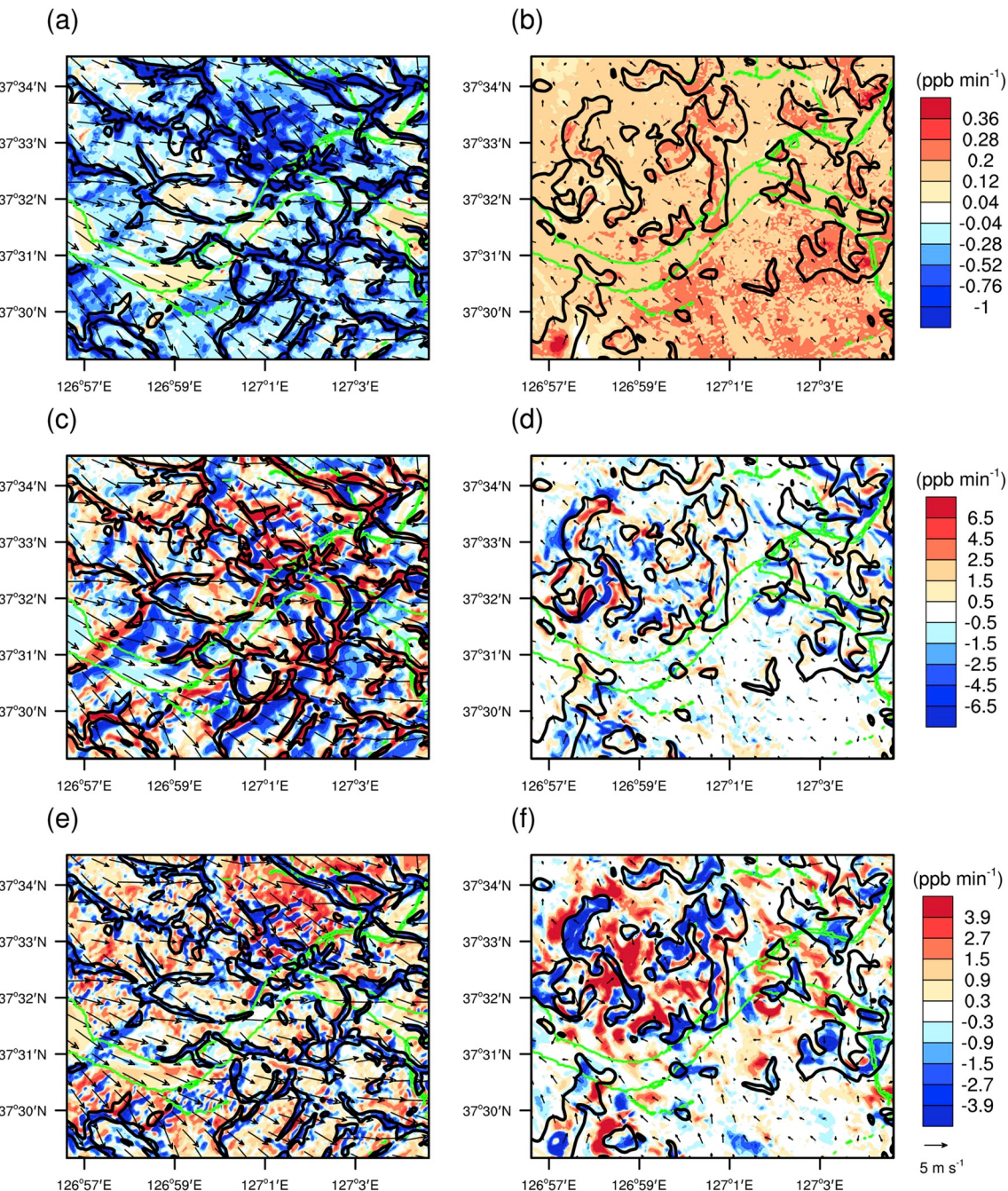


**Fig. 10.** Fields of the contributions of (a, b) chemical process, (c, d) horizontal advection process, and (e, f) vertical advection process to O<sub>3</sub> concentration and wind vector at the second lowest model level (left panels,  $z \sim 100$  m) and 36th model level (right panels,  $z \sim 1.7$  km) at 1500 LT. The black contour lines represent the contours of vertical velocity with  $0.5\text{ m s}^{-1}$ . The green lines indicate the Han River and its tributaries. (For interpretation of the references to colour in this figure legend, the reader is referred to the Web version of this article.)

square error, and correlation do not change much when the horizontal model resolution increases; that is, the increase of the horizontal model resolution does not significantly affect the model performance in simulating O<sub>3</sub> in this study. For NO<sub>2</sub> concentration, the model performance is improved when the horizontal model resolution increases from 1.25 km to 0.25 km. The magnitudes of the mean bias and root-mean-square error of the simulated NO<sub>2</sub> concentration are decreased, and the correlation is increased. However, there are no significant differences between the mean biases, root-mean-square errors, and correlations calculated using the simulated NO<sub>2</sub> concentrations in the 0.25 km and 50 m domains. It seems that the increase of the horizontal model resolution from 0.25 km to 50 m does not significantly affect the model

performance in simulating NO<sub>2</sub> in this study. The overall results show that when the horizontal model resolution is increased, the model performance may not always improve. We expect to investigate why this is so and how to best approach this performance issue in a future study.

The effects of the horizontal model resolution on the characteristics of turbulent coherent structures and air quality are also investigated. Vertical O<sub>3</sub> concentration profiles at the location of Jung-gu AQMS (the yellow dot in Fig. 1b, located in a highly urbanized area) from the simulation results of the 1.25 km, 0.25 km, and 50 m domains are shown in Fig. 9. At 0900 LT, the differences between the vertical O<sub>3</sub> concentration profiles of the 1.25 km, 0.25 km, and 50 m domains are small. At 1500 LT, the differences between the vertical O<sub>3</sub> concentration profiles

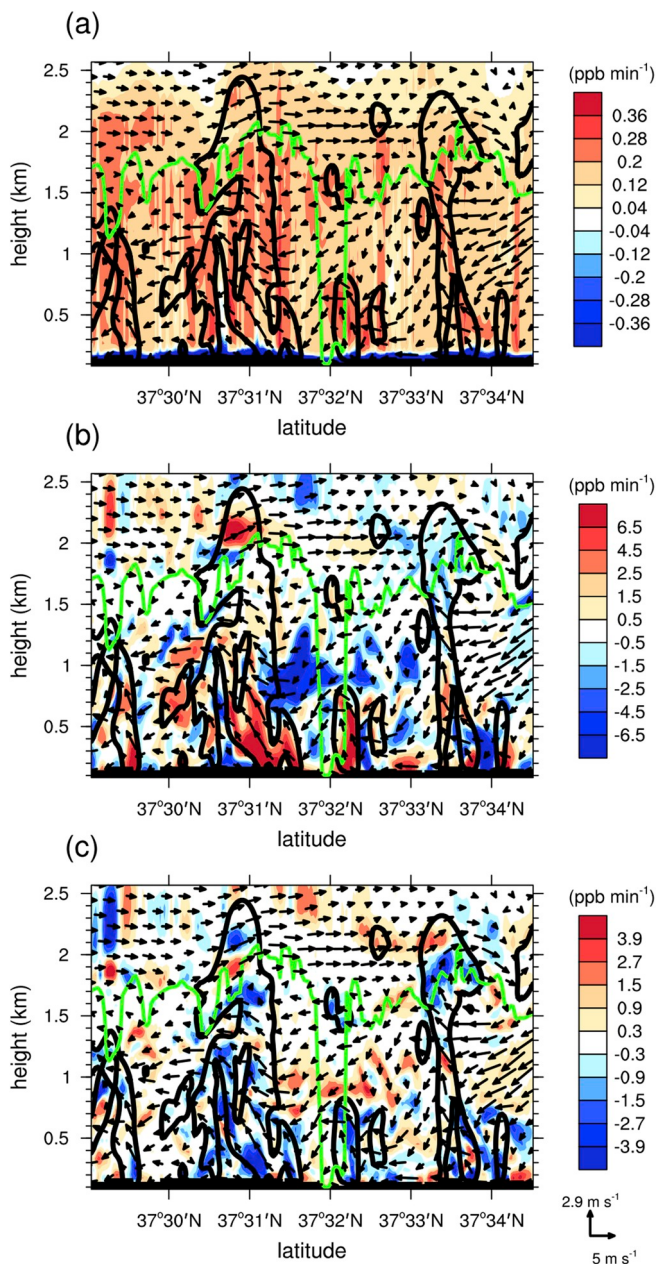


**Fig. 11.** Vertical cross-sections of the contributions of (a) chemical process, (b) horizontal advection process, and (c) vertical advection process to  $O_3$  concentration and wind vector along the black solid line in Fig. 1b at 1500 LT. The black contour lines represent the contours of vertical velocity with  $0.5 \text{ m s}^{-1}$ , and the green lines indicate the PBL height. (For interpretation of the references to colour in this figure legend, the reader is referred to the Web version of this article.)

of the 1.25 km, 0.25 km, and 50 m domains are large, implying that the effects of the turbulent flows (updrafts related to convective structures and eddies at the PBL top) on  $O_3$  concentration vary depending on the horizontal model resolution. In particular,  $O_3$  concentration above  $z \sim 2.1 \text{ km}$  in the 50 m domain is larger than those in the 1.25 km and 0.25 km domains because  $O_3$  precursors are transported upward by updrafts related to convective structures and eddies at the PBL top which are resolved well in the 50 m domain.

### 3.2. Process analysis

To evaluate the effects of convective structures on the contributions

of individual processes to  $O_3$  concentration, an integrated process rate (IPR) analysis (Gipson, 1999) is performed. The IPR analysis quantifies the contributions of individual processes, such as chemical, advection, and diffusion processes, to pollutant concentration (Jeffries and Tonnesen, 1994). Fig. 10 shows fields of the contributions of chemical, horizontal advection, and vertical advection processes to  $O_3$  concentration and horizontal wind vector at 1500 LT. The left and right panels of Fig. 10 show the process analysis results near the surface (the second lowest model level,  $z \sim 100 \text{ m}$ ) and slightly above the PBL top (the 36th model level,  $z \sim 1.7 \text{ km}$ ), respectively. At this time, the domain-averaged PBL height is  $\sim 1.5 \text{ km}$ . The black contour lines represent the contours of vertical velocity with  $0.5 \text{ m s}^{-1}$ . At the second lowest model level, the magnitude of the negative contribution of the chemical process in updraft areas is larger than that in other areas because updrafts transport air at lower level, which has higher  $NO_x$  concentration than air at upper level, inducing  $O_3$  decomposition (Fig. 10a). When air in other areas is transported to updraft areas, the positive contribution of the horizontal advection process generally appears in updraft areas because  $O_3$  concentration in updraft areas is lower than that in other areas, as shown in Fig. 5 (Fig. 10c). The negative contribution of the vertical advection process appears in updraft areas because updrafts transport air at lower level upward, which has lower  $O_3$  concentration than air at upper level (Fig. 10e).

Slightly above the PBL top, the magnitude of the positive contribution of the chemical process in updraft areas is generally larger than that in other areas due to the transport of  $O_3$  precursors at lower level (e.g.,  $NO_x$ ) (Fig. 10b). The contribution of the horizontal advection process around updraft areas is generally negative because air with low  $O_3$  concentration diverges from updraft areas (Fig. 10d). For example, a divergent flow and the associated negative contribution of the horizontal advection process appear clearly in an updraft area located at ( $\sim 127^\circ 3.7' \text{E}$ ,  $\sim 37^\circ 34.0' \text{N}$ ). The contribution of the vertical advection process in updraft areas is generally negative, similar to that at the second lowest model level (Fig. 10f). In contrast, the contribution of the vertical advection process around updraft areas is generally positive because the maximum  $O_3$  concentration at 1500 LT appears at  $z \sim 1.8 \text{ km}$  and downdrafts around updraft areas transport air with high  $O_3$  concentration at and near  $z = 1.8 \text{ km}$  downward.

Fig. 11 shows the vertical cross-sections of the contributions of chemical, horizontal advection, and vertical advection processes to  $O_3$  concentration and wind vector along the black solid line in Fig. 1b at 1500 LT. In the region between  $z \sim 0.2 \text{ km}$  and the PBL top, the contribution of the chemical process is generally positive (Fig. 11a). In particular, the large positive contribution of the chemical process generally appears in updraft areas (e.g., updrafts at  $37^\circ 31.2' \text{N}$ ) due to the transport of  $O_3$  precursors, as shown in Fig. 10. Since these updrafts and clockwise-rotating eddies at the PBL top transport  $O_3$  precursors above the PBL top, the contribution of the chemical process above the PBL top is also positive. Due to the positive contribution of the chemical process above the PBL top, the maximum  $O_3$  concentration at 1500 LT appears slightly above the PBL top (Fig. 8). Below the PBL top, the contributions of the horizontal and vertical advectives are generally positive and negative in updraft areas (e.g., updrafts at  $37^\circ 31.2' \text{N}$  and  $37^\circ 32.2' \text{N}$ ), respectively, as shown in Fig. 10 (Fig. 11b and c). Above the PBL top, the mixing of air by clockwise-rotating eddies at the PBL top affects the contribution of the vertical advection process. For example, updraft of the eddy at  $37^\circ 33.8' \text{N}$  transports air just below the PBL top upward. Since  $O_3$  concentration at 1500 LT is highest slightly above the PBL top, the transport of air from just below the PBL top to slightly above the PBL top causes the negative contribution of the vertical advection process. These results clearly show that clockwise-rotating eddies at the PBL top mix air above the PBL top with air below it.

To quantitatively compare the contributions of individual processes to  $O_3$  concentration in updraft and downdraft areas, temporally- and area-averaged vertical profiles of the contributions of chemical, vertical advection, horizontal advection, and total diffusion processes to  $O_3$

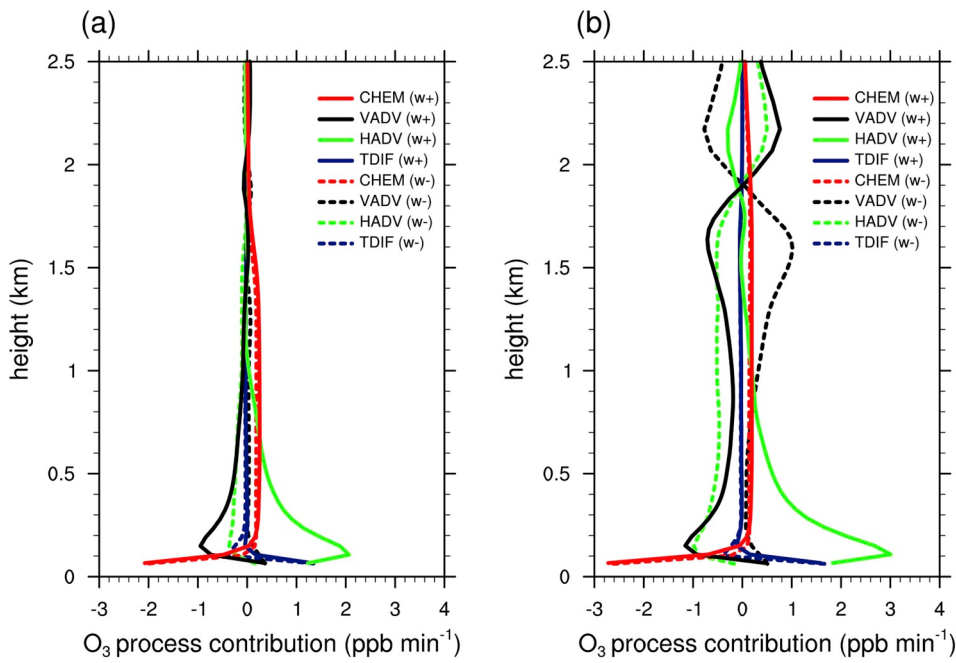


**Fig. 12.** Vertical profiles of the contributions of chemical (CHEM), vertical advection (VADV), horizontal advection (HADV), and total diffusion (TDIF) processes to O<sub>3</sub> concentration averaged over updraft areas larger than 0.1 m s<sup>-1</sup> (w+) and downdraft areas smaller than -0.1 m s<sup>-1</sup> (w-) and the period (a) from 1145 LT to 1215 LT and (b) from 1445 to 1515 LT. The solid and dashed lines represent the contributions in updraft and downdraft areas, respectively. (For interpretation of the references to colour in this figure legend, the reader is referred to the Web version of this article.)

concentration for the period from 1145 LT to 1215 LT and from 1445 LT to 1515 LT are shown in Fig. 12. Here, the total diffusion process indicates the sum of the horizontal and vertical diffusion processes.

For the period from 1145 LT to 1215 LT, the positive contribution of the chemical process averaged over updraft areas is larger than that averaged over downdraft areas above  $z \sim 0.2$  km due to the upward O<sub>3</sub> precursor transport (Fig. 12a). Below  $z \sim 1.5$  km (near the PBL top at 1200 LT), the contribution of the vertical advection process averaged over updraft areas is negative except near the surface due to the upward transport of air at lower level, which has lower O<sub>3</sub> concentration than air at upper level. The contribution of the horizontal advection process averaged over updraft areas for the period from 1145 LT to 1215 LT is positive below  $z \sim 1$  km because of the low O<sub>3</sub> concentration in updraft areas. In contrast, the contribution of the horizontal advection process averaged over downdraft areas is negative except near the surface. Above  $z \sim 1.5$  km, the contributions of the horizontal and vertical advection processes averaged over updraft and downdraft areas are close to zero because turbulent flows above the PBL top are weak.

For the period from 1445 LT to 1515 LT, similar characteristics are seen in the temporally- and area-averaged contributions of the chemical, horizontal advection, and vertical advection processes at lower level, except that the magnitudes of the temporally- and area-averaged contributions of the horizontal advection process are increased (Fig. 12b). This is because the difference between the area-averaged O<sub>3</sub> concentrations in updraft areas and other areas increases. The magnitudes of the temporally- and area-averaged contributions of the horizontal and vertical advection processes are generally larger than those for the period from 1145 LT to 1215 LT. This is because convective structures are strengthened, vertical motions at and near the PBL top are enhanced, and clockwise-rotating eddies at the PBL top appear more frequently. Above  $z \sim 1.9$  km, the contribution of the vertical advection process averaged over updraft areas is positive. For the period from 1445 LT to 1515 LT, the maximum O<sub>3</sub> concentration appears at  $z \sim 1.9$  km, thus upward transport of air at  $z \sim 1.9$  km induces the positive contribution of the vertical advection process. Similar results are seen in the contribution of the vertical advection process averaged over downdraft areas, except that the sign of the contribution of the vertical advection process averaged over downdraft areas is opposite to that averaged over updraft areas.

#### 4. Summary and conclusions

We investigated the effects of turbulent coherent structures on daytime ozone air quality in a megacity, Seoul. To resolve turbulent coherent structures, the WRF-CMAQ model simulation with a very high resolution (50 m) is performed in this study. In the daytime, westerly to northwesterly sea breeze appears. Also, surface heating increases the temperature of air near the surface, and the heated air rises upward and forms a convective structure. Eddies at the PBL top are formed when updrafts related to convective structures reach above the PBL top. Updrafts related to convective structures transport air at lower level upward, which has higher NO<sub>x</sub> and lower O<sub>3</sub> concentrations than air at upper level. Eddies at the PBL top mix air above and below the PBL top. Due to the upward transport of O<sub>3</sub> precursors and low wind speed at and near the PBL top, O<sub>3</sub> is chemically produced and accumulated at and near the PBL top in the afternoon. In the late afternoon, convection and associated vertical motions in Seoul are weakened and eddies at the PBL top do not appear. The process analysis also shows the impacts of turbulent coherent structures on O<sub>3</sub> concentration in the afternoon. Below  $z \sim 0.1$  km, the chemical decomposition of O<sub>3</sub> occurs actively in updraft areas because of the upward transport of air at lower level, which has higher NO<sub>x</sub> concentration than air at upper level. Since O<sub>3</sub> concentration in updraft areas is generally lower than that in other areas, the horizontal advection from other areas to updraft areas increases O<sub>3</sub> concentration in updraft areas. Slightly above the PBL top, O<sub>3</sub> is chemically produced in updraft areas because of the O<sub>3</sub> precursor transport by updrafts. The negative contribution of the horizontal advection process appears around updraft areas due to the divergent air with low O<sub>3</sub> concentration from updraft areas. On the other hand, the positive contribution of the vertical advection process appears around updraft areas because downdrafts around updraft areas transport air with high O<sub>3</sub> concentration above the PBL top downward. The magnitudes of the contributions of the horizontal and vertical advection processes are increased as convective structures are strengthened, vertical motions at and near the PBL top are enhanced, and eddies at the PBL top appear more frequently.

This study considered only one case. Turbulent coherent structures can differ depending on weather conditions. It would be interesting to examine how the impacts of turbulent coherent structures on pollutant concentrations vary under different weather conditions. The effects of

long-range transport can be additionally considered in a future study with a longer simulation time. This study shows that the spatial and temporal variations of pollutant concentrations in urban areas can be strongly influenced by turbulent coherent structures. To better understand and more accurately predict urban air quality, it is necessary to take account of turbulent coherent structures. We expect follow-up studies on turbulent coherent structures and air quality in urban areas using high-resolution models.

## Declaration of competing interest

The authors declare that they have no known competing financial interests or personal relationships that could have appeared to influence the work reported in this paper.

## Acknowledgements

The authors are grateful to the anonymous reviewers for providing valuable comments on this work. This work was supported by Basic Science Research Program through the National Research Foundation of Korea (NRF) funded by the Ministry of Science and ICT (No. 2016R1A2B2013549).

## References

- Appel, K.W., Pouliot, G.A., Simon, H., Sarwar, G., Pye, H.O.T., Napelenok, S.L., Akhtar, F., Roselle, S.J., 2013. Evaluation of dust and trace metal estimates from the Community Multiscale Air Quality (CMAQ) model version 5.0. *Geosci. Model Dev.* 6, 883–899.
- Byun, D., Schere, K.L., 2006. Review of the governing equations, computational algorithms, and other components of the models-3 community multiscale air quality (CMAQ) modeling system. *Appl. Mech. Rev.* 59, 51–77.
- Carter, W.P.L., 2010. Development of a condensed SAPRC-07 chemical mechanism. *Atmos. Environ.* 44, 5336–5345.
- Chen, F., Dudhia, J., 2001. Coupling an advanced land surface–hydrology model with the Penn State–NCAR MM5 modeling system. Part I: model implementation and sensitivity. *Mon. Weather Rev.* 129, 569–585.
- Civerolo, K., Hogrefe, C., Lynn, B., Rosenthal, J., Ku, J.-Y., Solecki, W., Cox, J., Small, G., Rosenzweig, C., Goldberg, R., Knolton, K., Kinney, P., 2007. Estimating the effects of increased urbanization on surface meteorology and ozone concentrations in the New York City metropolitan region. *Atmos. Environ.* 41, 1803–1818.
- Cuchiara, G.C., Rappenglück, B., 2018. Performance analysis of WRF and LES in describing the evolution and structure of the planetary boundary layer. *Environ. Fluid Mech.* 18, 1257–1273.
- Deardorff, J.W., 1980. Stratocumulus-capped mixed layers derived from a three-dimensional model. *Boundary-Layer Meteorol.* 18, 495–527.
- Dudhia, J., 1989. Numerical study of convection observed during the winter monsoon experiment using a mesoscale two-dimensional model. *J. Atmos. Sci.* 46, 3077–3107.
- Farr, T.G., Rosen, P.A., Caro, E., Crippen, R., Duren, R., Hensley, S., Kobrick, M., Paller, M., Rodriguez, E., Roth, L., Seal, D., Shaffer, S., Shimada, J., Umland, J., Werner, M., Oskin, M., Burbank, D., Alsdorf, D., 2007. The shuttle radar topography mission. *Rev. Geophys.* 45.
- Gipson, G.L., 1999. Science Algorithms of the EPA Models-3 Community Multiscale Air Quality (CMAQ) Modeling System: Process Analysis, p. 37. EPA/600/R-99/030. US EPA.
- Guenther, A., Karl, T., Harley, P., Wiedinmyer, C., Palmer, P.I., Geron, C., 2006. Estimates of global terrestrial isoprene emissions using MEGAN (model of emissions of gases and aerosols from nature). *Atmos. Chem. Phys.* 6, 3181–3210.
- Han, B.-S., Baik, J.-J., Park, S.-B., Kwak, K.-H., 2019. Large-eddy simulation of reactive pollutant dispersion in the convective boundary layer over flat and urban-like surfaces. *Boundary-Layer Meteorol.* 172, 271–289.
- Hogrefe, C., Hao, W., Civerolo, K., Ku, J.-Y., Sistla, G., Gaza, R., Sedefian, L., Schere, K., Gilliland, A., Mathur, R., 2007. Daily simulation of ozone and fine particulates over New York State: findings and challenges. *J. Appl. Meteorol. Climatol.* 46, 961–979.
- Hong, S.-Y., Lim, J.-O.J., 2006. The WRF single-moment 6-class microphysics scheme (WSM6). *J. Korean Meteor. Soc.* 42, 129–151.
- Hong, S.-Y., Noh, Y., Dudhia, J., 2006. A new vertical diffusion package with an explicit treatment of entrainment processes. *Mon. Weather Rev.* 134, 2318–2341.
- Houyoux, M.R., Vukovich, J.M., Coats Jr., C.J., Wheeler, N.J.M., Kasibhatla, P.S., 2000. Emission inventory development and processing for the seasonal model for regional air quality (SMRAQ) project. *J. Geophys. Res.* 105, 9079–9090.
- Jeffries, H.E., Tonnesen, S., 1994. A comparison of two photochemical reaction mechanisms using mass balance and process analysis. *Atmos. Environ.* 28, 2991–3003.
- Kain, J.S., 2004. The Kain–Fritsch convective parameterization: an update. *J. Appl. Meteorol.* 43, 170–181.
- Kim, S., Moon, N., Byun, D.W., 2008. Korea emissions inventory processing using the US EPA's SMOKE system. *Asian J. Atmos. Environ.* 2, 34–46.
- Loughner, C.P., Allen, D.J., Pickering, K.E., Zhang, D.-L., Shou, Y.-X., Dickerson, R.R., 2011. Impact of fair-weather cumulus clouds and the Chesapeake Bay breeze on pollutant transport and transformation. *Atmos. Environ.* 45, 4060–4072.
- Loughner, C.P., Tzortziou, M., Follette-Cook, M., Pickering, K.E., Goldberg, D., Satam, C., Weinheimer, A., Crawford, J.H., Knapp, D.J., Montzka, D.D., Diskin, G.S., Dickerson, R.R., 2014. Impact of bay-breeze circulations on surface air quality and boundary layer export. *J. Appl. Meteorol. Climatol.* 53, 1697–1713.
- Lee, D.G., Lee, Y.-M., Jang, K.-W., Yoo, C., Kang, K.-H., Lee, J.-H., Jung, S.-W., Park, J.-M., Lee, S.-B., Han, J.-S., Hong, J.-H., Lee, S.-J., 2011. Korean national emissions inventory system and 2007 air pollutant emissions. *Asian J. Atmos. Environ.* 5, 278–291.
- Lee, S.-H., Kim, S., 2015. Estimation of anthropogenic heat emission over South Korea using a statistical regression method. *Asia-Pac. J. Atmos. Sci.* 51, 157–166.
- Mao, J., Ren, X., Chen, S., Brune, W.H., Chen, Z., Martinez, M., Harder, H., Lefer, B., Rappenglück, B., Flynn, J., Leuchner, M., 2010. Atmospheric oxidation capacity in the summer of Houston 2006: comparison with summer measurements in other metropolitan studies. *Atmos. Environ.* 44, 4107–4115.
- Mlawer, E.J., Taubman, S.J., Brown, P.D., Iacono, M.J., Clough, S.A., 1997. Radiative transfer for inhomogeneous atmospheres: RRTM, a validated correlated-k model for the longwave. *J. Geophys. Res.* 102, 16663–16682.
- Moeng, C.-H., 1984. A large-eddy-simulation model for the study of planetary boundary-layer turbulence. *J. Atmos. Sci.* 41, 2052–2062.
- Moon, N., Kim, S., Byun, D.W., Joe, Y., 2006. Air Quality Modeling System I – Development of Emissions Preparation System with the CAPSS. Korea Environment Institute, Report 2006-RE-11.
- Rai, R.K., Berg, L.K., Kosović, B., Mirocha, J.D., Pekour, M.S., Shaw, W.J., 2017. Comparison of measured and numerically simulated turbulence statistics in a convective boundary layer over complex terrain. *Boundary-Layer Meteorol.* 163, 69–89.
- Ryu, Y.-H., Baik, J.-J., Kwak, K.-H., Kim, S., Moon, N., 2013. Impacts of urban land-surface forcing on ozone air quality in the Seoul metropolitan area. *Atmos. Chem. Phys.* 13, 2177–2194.
- Ryu, Y.-H., Baik, J.-J., Lee, S.-H., 2011. A new single-layer urban canopy model for use in mesoscale atmospheric models. *J. Appl. Meteorol. Climatol.* 50, 1773–1794.
- Ryu, Y.-H., Baik, J.-J., 2013. Daytime local circulations and their interactions in the Seoul metropolitan area. *J. Appl. Meteorol. Climatol.* 52, 784–801.
- Ryu, Y.-H., Baik, J.-J., Lee, S.-H., 2013. Effects of anthropogenic heat on ozone air quality in a megacity. *Atmos. Environ.* 80, 20–30.
- Schumann, U., 1989. Large-eddy simulation of turbulent diffusion with chemical reactions in the convective boundary layer. *Atmos. Environ.* 23, 1713–1727.
- Skamarock, W.C., Klemp, J.B., Dudhia, J., Gill, D.O., Barker, D.M., Duda, M.G., Huang, X.-Y., Wang, W., Powers, J.G., 2008. A Description of Advanced Research WRF Version 3. NCAR Technical Note NCAR/TN-475+STR.
- Stauffer, R.M., Thompson, A.M., Martins, D.K., Clark, R.D., Goldberg, D.L., Loughner, C.P., Delgado, R., Dickerson, R.R., Stehr, J.W., Tzortziou, M., 2015. Bay breeze influence on surface ozone at Edgewood, MD during July 2011. *J. Atmos. Chem.* 72, 335–353.
- Sullivan, J.T., Timothy, B., Guillaume, G., Travis, K., Margaret, P., Danette, A., Laurence, T., Berkoff, T., Gronoff, G., Knepp, T., Pippin, M., Allen, D., Twigg, L., Swap, R., Tzortziou, M., Thompson, A.M., Stauffer, R.M., Wolfe, G.M., Flynn, J., Pusede, S.E., Judd, L.M., Moore, W., Baker, B.D., Al-Saadi, J., McGee, T.J., 2019. The ozone water-land environmental transition study: an innovative strategy for understanding Chesapeake Bay pollution events. *Bull. Am. Meteorol. Soc.* 100, 291–306.
- Tao, H., Xing, J., Zhou, H., Chang, X., Li, G., Chen, L., Li, J., 2018. Impacts of land use and land cover change on regional meteorology and air quality over the Beijing-Tianjin-Hebei region, China. *Atmos. Environ.* 189, 9–21.
- Vila-Guerau de Arellano, J., Dosio, A., Vinuesa, J.F., Holtslag, A.A.M., Galmarini, S., 2004. The dispersion of chemically reactive species in the atmospheric boundary layer. *Meteorol. Atmos. Phys.* 87, 23–38.
- Zaveri, R.A., Berkowitz, C.M., Kleinman, L.I., Springston, S.R., Doskey, P.V., Lonneman, W.A., Spicer, C.W., 2003. Ozone production efficiency and NO<sub>x</sub> depletion in an urban plume: interpretation of field observations and implications for evaluating O<sub>3</sub>–NO<sub>x</sub>-VOC sensitivity. *J. Geophys. Res.* 108 <https://doi.org/10.1029/2002JD003144>.
- Zhang, F., Bei, N., Nielsen-Gammon, J.W., Li, G., Zhang, R., Stuart, A., Aksoy, A., 2007. Impacts of meteorological uncertainties on ozone pollution predictability estimated through meteorological and photochemical ensemble forecasts. *J. Geophys. Res.* 112 <https://doi.org/10.1029/2006JD007429>.
- Zhang, Y.H., Su, H., Zhong, L.J., Cheng, Y.F., Zeng, L.M., Wang, X.S., Xiang, Y.R., Wang, J.L., Gao, D.F., Shao, M., Fan, S.J., Liu, S.C., 2008. Regional ozone pollution and observation-based approach for analyzing ozone–precursor relationship during the PRIDE-PRD2004 campaign. *Atmos. Environ.* 42, 6203–6218.